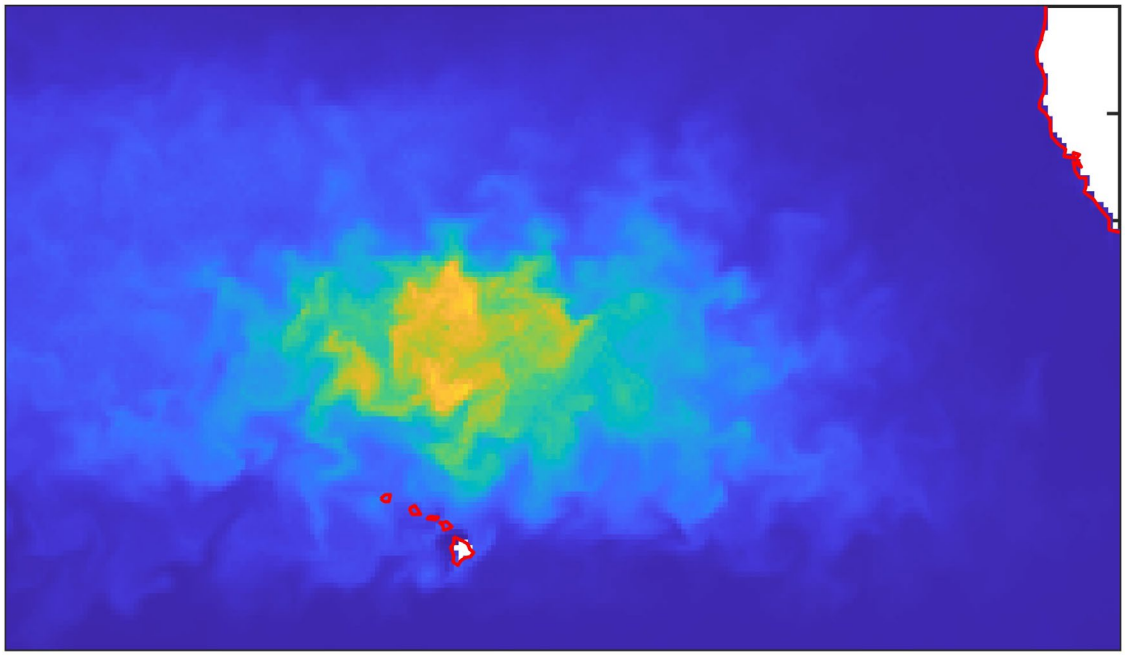
SCHOOL OF OCEAN AND EARTH SCIENCE AND TECHNOLOGY
UNIVERSITY OF HAWAI'I AT MĀNOA

INTERNATIONAL PACIFIC RESEARCH CENTER



Near-real time model product to support marine debris research and operations in Hawaii and in the eastern North Pacific

Nikolai Maximenko and Jan Hafner

IPRC Technical Note No. 7
October 20, 2024

Sea Grant
UNIVERSITY OF HAWAI'I

NASA
Partner

Table of contents

page

1. **Accumulation of anthropogenic marine debris in the North Pacific garbage patch** ……. 3
2. **Model setup**……. 3
   - *2.1 Problems*
   - *2.2 The concept of "old" debris*
   - *2.3 Model dynamics and wind coefficients*
   - *2.4 Domain, grid, sources & sinks*
   - *2.5 Model forcing*
   - *2.6 Lagrangian scheme*
3. **Model saturation run**…….. 8
4. **Near-real time product**…… 11
   - *4.1 Access to the Google Drive and folder structure*
   - *4.2 Algorithm for updates*
   - *4.3 Island indices*
5. **Utility and limitations of the product**…… 14
6. **Feedback and requests**…… 15
7. **Acknowledgements**…….. 15
8. **Citation**……. 15
9. **References**…… 16

1. Accumulation of anthropogenic marine debris in the North Pacific garbage patch.

The invention of plastic materials and their broad introduction to the market of goods had an unexpected impact on the environment. These cheap and durable materials often avoid the waste treatment systems and gradually accumulate in nature. The presence of plastic pollution is especially visible in remote areas of the ocean where other impacts of human activities are relatively weak.

Floating debris, carried by currents and winds disperses over vast areas. Its concentration is not uniform and reaches maximum values in the five main "garbage patches", all located in the subtropical oceans (e.g., Maximenko et al, 2012). In Hawaii, most debris come from the garbage patch fed by remote sources scattered over the North Pacific.

Here, we developed a model product that reproduces main properties of the North Pacific garbage patch and predicts the influx of "old" debris on Hawaiian shorelines.

2 Model setup

2.1 Problems

Modeling of the garbage patch faces several difficult problems.

First, the spatial and temporal distributions of sources of marine debris on land and at sea are largely unknown and marine debris observing systems such as IMDOS (Maximenko et al., 2019, Maximenko et al. 2021) are still in their infancy.

Second, the dynamics of marine debris (i.e. how it moves under the force of ocean currents, winds, and waves) are not well known and objects of different geometry (windage) move differently. As a result, even the best ocean general circulation models (OGCMs) can produce controversial or misleading results (Maximenko et al, 2018; Potemra, 2012).

Other unknowns include debris composition, degradation, and loss of buoyancy with time.

2.2 The concept of "old" debris

We assume that objects drifting on the ocean surface gradually mix with objects from other sources and "forget" their origin and history. Under this scenario, with time, ocean dynamics play a more and more important role in the formation of the spatial patterns of debris while the details of sources and pathways of individual items become unimportant.

2.3 Model dynamics and wind coefficients

The model used in this product is the next generation of the SCUD model (Maximenko and Hafner, 2010). Since its development, SCUD was used to simulate drift of debris from the 2011 tsunami in Japan (Maximenko et al., 2018) and in that study it outperformed three OGCMs (Ocean General Circulation Models). The weakness of SCUD, which urged for the update, is that the data of drifters with the drogues attached were mixed with the drifters that lost their drogues or were deployed without a drogue. The implication for such a mixture was expected the complex composition of

marine debris, including objects broadly ranging in dynamical properties. Maximenko et al (2018) showed that tsunami debris objects of different types took very different paths, suggesting that that a better focused model is necessary. Trinanes et al (2016) analyzed the probable trajectory of the flaperon from the flight MH370 of Malaysian Airlines. The airplane disappeared in 2014 in the Southern Indian Ocean and the flaperon and some other debris were later found on Reunion Island. The study showed that debris followed the path commonly taken by undrogued drifters.

During the FloatEco[1] (Floating Ocean Ecosystems) experiment the drift dynamics of floating objects of various geometry revealed that movement of derelict fishing gear tagged by the Ocean Voyages Institute (a joint paper in preparation) with GPS trackers corresponded (in terms of its response to the local wind) to the drift of a standard undrogued drifter of the Global Drifter Program.

Similarly to SCUD, the main assumption of the new model is that the dominant physics controlling low-frequency velocities of an object drifting on the ocean surface include geostrophic dynamics and wind-induced movement, the latter including the Ekman currents, Stokes drift, and downwind slip induced by the direct wind force applied to the above-surface parts of the object.

A new methodology was developed for calculations of wind coefficients. In SCUD, drifter velocity components were linearly regressed to the components of geostrophic velocity and wind vectors and then analyzed to demonstrate that geostrophic currents do not require scaling and that the wind response matrix is close to rotational. The new model is developed in the framework of these findings and it assumes that ageostrophic velocities can be described by rotation and scaling of the wind vector and the coefficient does not depend on the wind direction. Trajectories of all undrogued drifters were extracted from the Global Drifter Program 6-hourly data archive ending March 2023 and the AVISO absolute geostrophic velocities and ERA5 winds (described in Section 2.5) were interpolated in space and time for every drifter fix.

Drifter velocities were then calculated by differentiating coordinates over 12 hours increment and approximated (in the complex notation) with

$$\mathbf{V_d} = \mathbf{V_g} + \mathbf{C} \cdot \mathbf{V_w}, \qquad (1)$$

where $\mathbf{V_d} = U_d + \mathbf{i} \cdot V_d$, $\mathbf{V_g} = U_g + \mathbf{i} \cdot V_g$, and $\mathbf{V_w} = U_w + \mathbf{i} \cdot V_w$ are collocated drifter, geostrophic, and wind velocities.

Optimal wind coefficients were calculated as

$$\mathbf{C} = < (\mathbf{V_d} - \mathbf{V_g}) \cdot conj(\mathbf{V_w}) > / < \mathbf{V_w} \cdot conj(\mathbf{V_w}) >, \qquad (2)$$

where *conj* is the conjugate operator. Eq. (2) is a complex version of the linear regression, minimizing the square difference between the left and right sides of Eq. (1). Importantly, unlike the methodology used in the original SCUD model, results of Eq. (2) are insensitive to the high-frequency signal and do not require low-pass filtering to remove currents associated with tides and

[1] https://www.floateco.org

inertial oscillations, which do not fit in the concept of Eq. (1). Brackets in Eq. (2) define the way how the data were averaged.

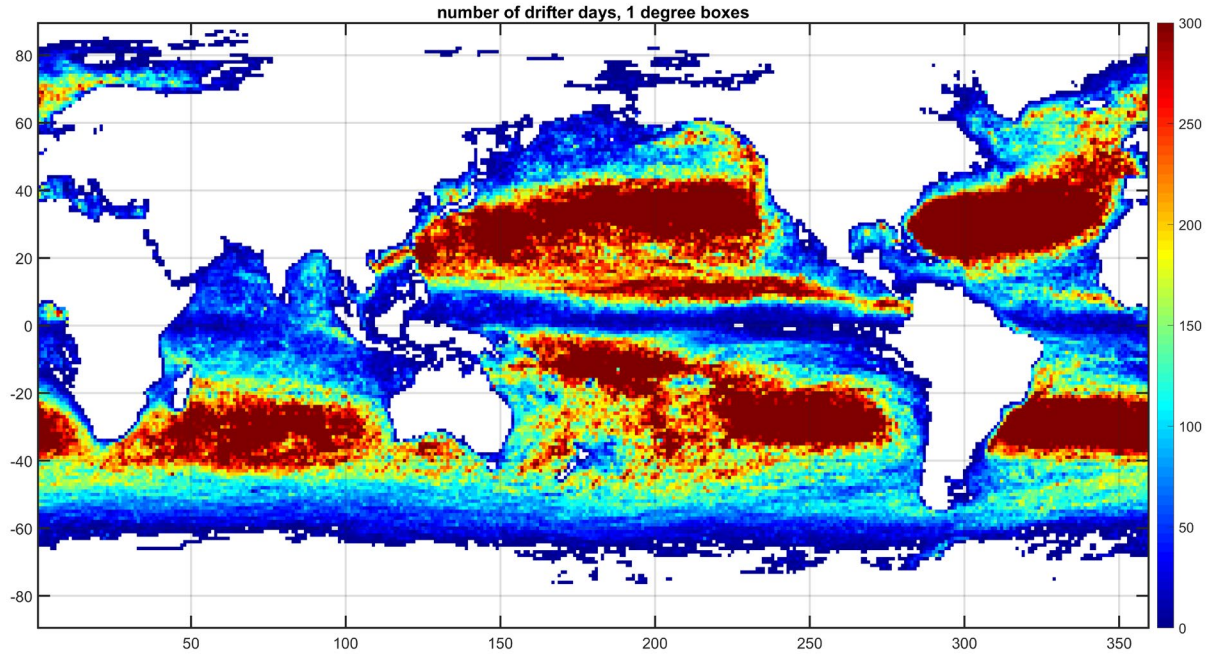


Figure 1. Spatial distribution of useful data in 1-degree bins. Units are drifter-days.

Uneven density of drifter data (Figure 1) required introduction of methodology that would compensate for the shortage of data in some areas, such as interpolation over gaps or increased radius of data included into local considerations. Most significant gaps exist outside of subtropical gyres: along the equator and at high latitudes. Preliminary calculations of wind coefficients within domains of various sizes revealed a strong "zonation" in the equatorial areas with large meridional and weak zonal gradients and relatively isotropic patterns at high latitude. After multiple experiments, we selected as a practical the method sorting the data within subdomains of $(2 \cdot R_x)$ by $(2 \cdot R_y)$ size and weighing the nominator and denominator of Eq. (2) with a two-dimensional cosine-filter with a half-width of R_x in the zonal direction and R_y in the meridional direction. The calculation was repeated for all subdomains with their centers coinciding with ocean grid points of the global ¼-degree grid. R_x and R_y varied with latitude as shown in Figure 2. The exact equations for scales are:

$$R_x=(1+1\cdot\exp(-\mathrm{abs}(y/10^0))\cdot 3.75^0,$$

$$R_y=(1-0.8\cdot\exp(-\mathrm{abs}(y)/10^0))\cdot 3.75^0. \qquad (3)$$

Thus, zonal scale varies from 7.5^0 on the equator to 3.75^0 at high latitudes while meridional scale grows from 0.75^0 on the equator to 3.75^0 at high latitudes.

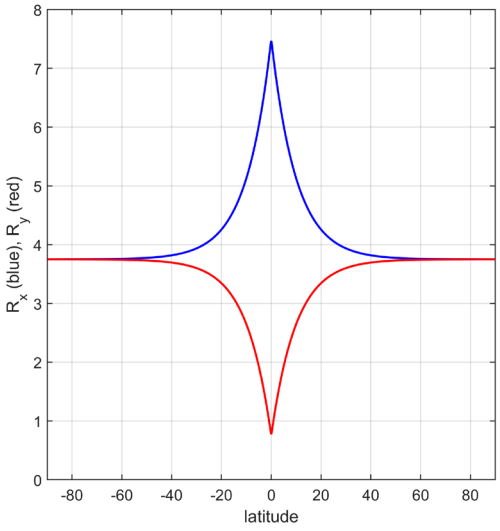


Figure 2. Zonal (R_x, blue) and meridional (R_y, red) scales of subdomains and filters used in calculations of wind coefficient. Units of the scales and latitude are degrees.

The resultant model wind coefficients are illustrated in Figures 3 and 4, showing that outside of the equatorial zone, the coefficients have a remarkably large-scale structure. Near the equator both the downwind and crosswind coefficients as well as the angle relative to the wind direction increase significantly. The crosswind coefficient and the angle are to the left of the wind direction in the northern hemisphere and to the right in the southern hemisphere. Figure 4 shows the complex coefficients as two-dimensional vectors and can be interpreted as tracer velocities under a unity eastward wind and no geostrophic currents.

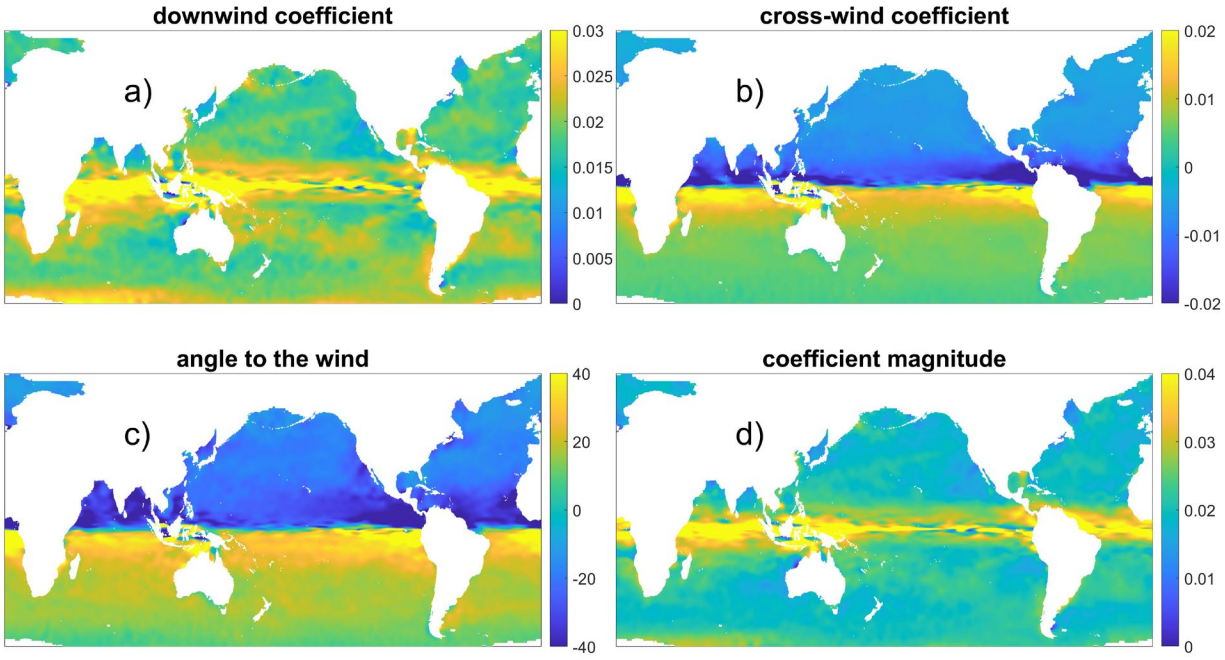


Figure 3. (a) Downwind and (b) crosswind coefficients. Coefficient (c) angle and (d) magnitude. Crosswind coefficient and angle are positive to the left from the wind direction. Coefficients are non-dimensional. Angle units are degrees.

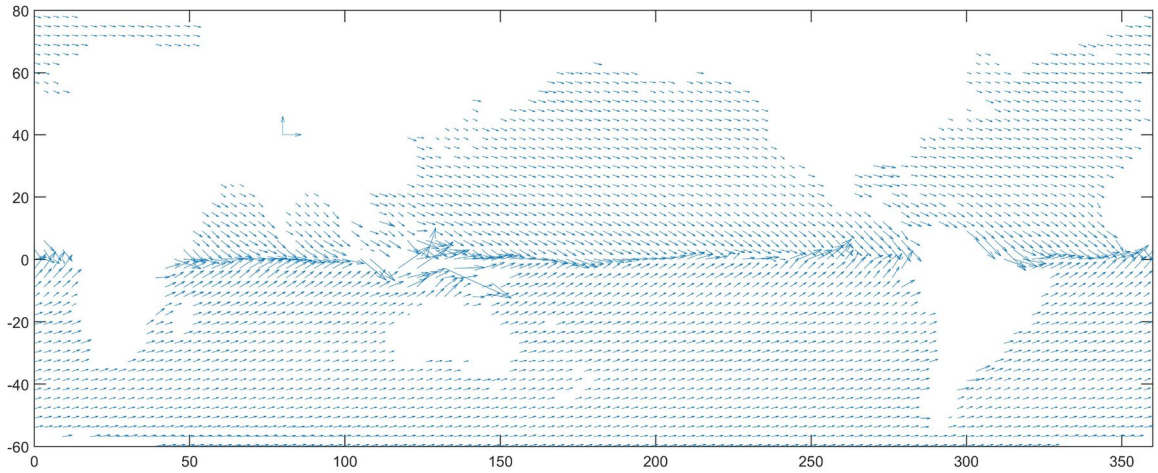


Figure 4. A quiver plot of wind coefficients, with an eastward/northward vector component representing the downwind/crosswind (to the left from the wind direction) coefficient. Vectors are plotted on a 3º x 3º grid. Vectors over Asia are plotted for the scale and represent downwind and crosswind coefficients of 0.05.

2.4 Domain, grid, sources & sinks

Under the easterly winds dominating the Equatorial Pacific, model wind coefficients (Figures 3 and 4) support strong divergence of model tracer at the equator and prevent or largely reduce the cross-equator tracer exchange. This allowed us to limit the model domain to the North Pacific.

Our model grid is ¼-degree in longitude and latitude, corresponding to the grids of wind and geostrophic velocity data used to force the model. The land mask (Figure 5) was derived from the ETOPO02 bathymetry by interpolating it to the model grid points.

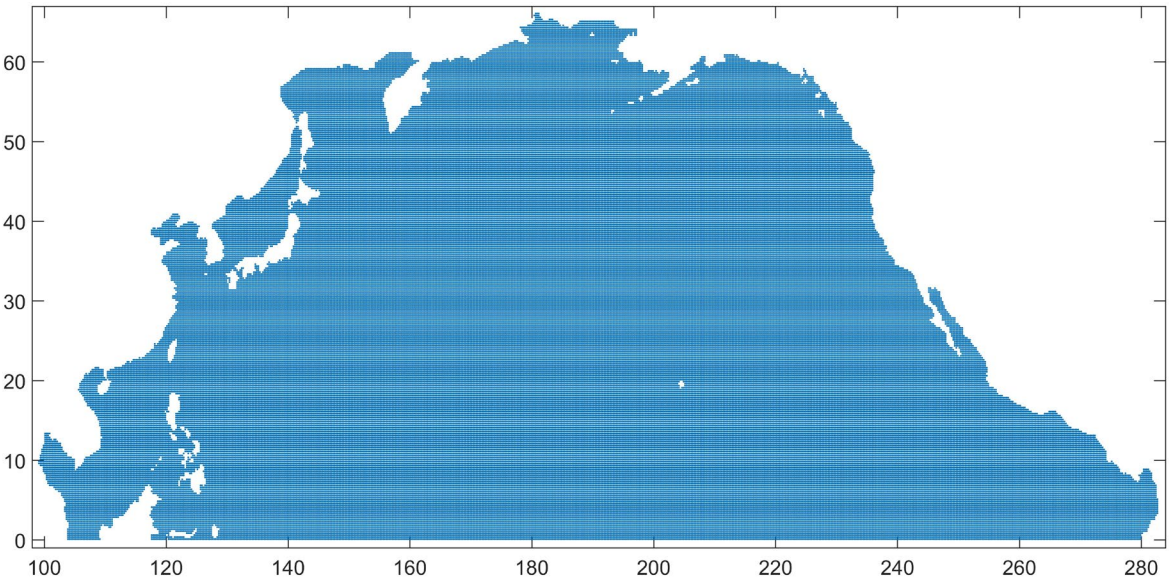


Figure 5. Model domain. Blue dots mark centers of ¼-degree ocean bins. White areas are treated as land.

Sources of model tracer are located at ocean model bins adjacent to the land bins and constant (a unity) amount of tracer is added to every source bin at every model time step. The sinks of the model tracer (the only way the tracer is removed from the model) are the land bins and also a row of bins just south of the equator. To allow model tracer to cross from the ocean to land bins, tracer velocities were interpolated over the land.

2.5 Model forcing

To derive tracer velocities, we used the following wind and geostrophic velocity products:

Absolute geostrophic velocities, derived from satellite altimetry products, were obtained from the AVISO (Archiving, Validation and Interpretation of Satellite Oceanographic[2]) data. The data are daily on a ¼-degree global grid and available, starting from October 1992, in near-real time and delayed modes. The 1993-2023 delayed mode data were used in saturation model experiments while near-real time data are used in daily updates of our product.

ERA5 10-meter wind velocities (Hersbach et al., 2023) were obtained from ECMWF (European Centre for Medium-Range Weather Forecasts). The data are hourly on a ¼-degree global grid and available freely with a six-day delay.

To fill the gap in ERA5 and to run a forecast, the GFS (Global Forecast System) 10-meter winds are obtained from the NOAA National Centers for Environmental Prediction[3] (NCEP). NOAA/NCEP Global Forecast System (GFS) Atmospheric Model). The GFS data have the same structure as ERA5.

2.6 Lagrangian scheme

The model solution is integrated using Lagrangian scheme. In every step, each ocean bin was subdivided into n by n equal areas and from the center of each area a particle was launched carrying c/n^2 tracer, where c is the amount of tracer in the ¼-degree model bin. Particle trajectories were integrated forward over a model step using the 2nd order Runge-Kutta scheme. Finally, corresponding amount of tracer was added to model bins (both ocean and land bins), in which the particles ended. In practice, we used n=15 and the model step equal to 1 day. Tracer in land and equatorial bins was counted separately and these bins were emptied on every step.

3. Model saturation run

The saturation experiment started from the zero (no tracer in the ocean) condition and spanned January 1, 1993 – December 31, 2023. At every 1-day step, a constant amount (a unity) of tracer was added to every near-shore bin and movement of tracer between the bins was calculated as described in Section 2.6.

As shown in Figure 6, in early model years the pattern of model tracer was defined by the pattern of near-shore sources but by the end of 1994 (only 2 years of simulation) coastal sources became

[2] https://www.aviso.altimetry.fr/en/data/products/sea-surface-height-products/global/gridded-sea-level-heights-and-derived-variables.html
[3] https://www.nco.ncep.noaa.gov/pmb/products/gfs/

less obvious and by the end of 1997 (5 years of simulation) the garbage patch started forming as an area of maximum tracer concentration in the eastern North Pacific.

After reaching December 31, 2023, the model was looped back to January 1, 1993. These cycles were repeated until the maximum difference between concentrations in the two consecutive cycles decreased to less than 1% of the maximum concentration. This criteria was met and simulation stopped after 7 full cycles.

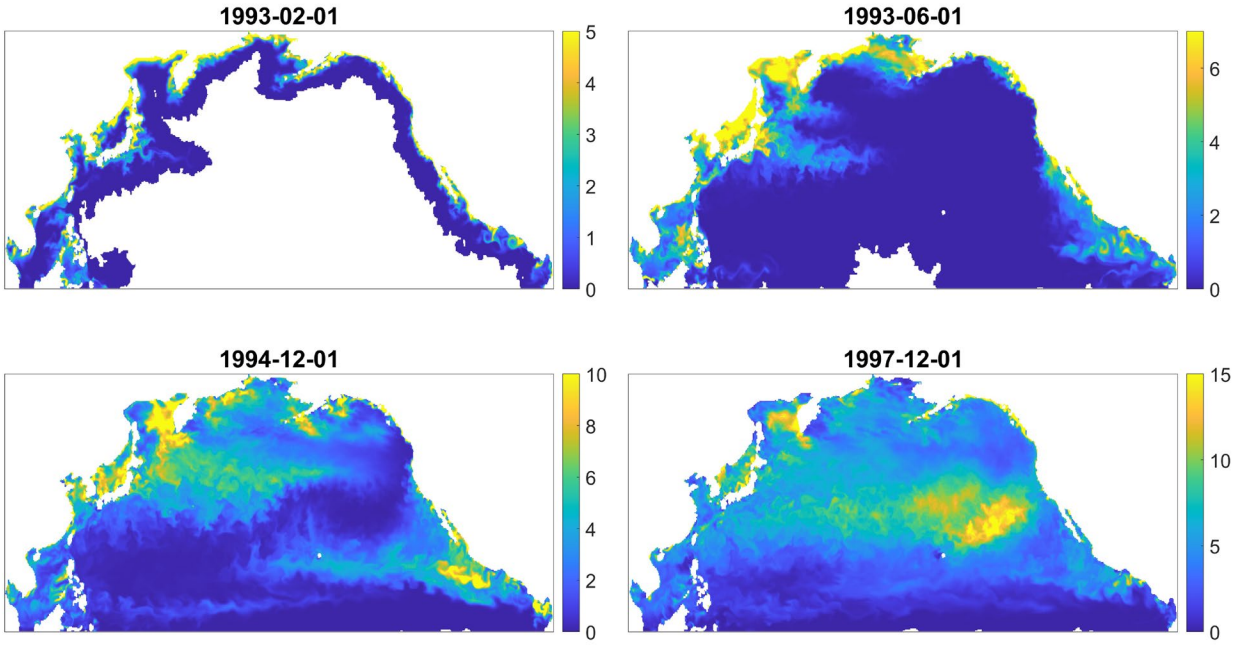


Figure 6. Evolution of the model solution in the 1st cycle of simulations. Note the changes in the color scales. Land and ocean pixels free from the tracer are masked in white. Note the emergence of the "garbage patch" by the end of 1997.

Convergence to the saturated solution is illustrated in Figures 7, 8, and 9, showing changes with model time in the total tracer content accumulating in the ocean and root-mean-squared (r.m.s.) differences between model solutions in pairs of consecutive cycles. By the end of cycle 7, the r.m.s. difference from cycle 6 was smaller than 5% of the mean tracer concentration.

The general spatial pattern of the tracer saturates even faster than the absolute values of concentration. Figure 10 shows that by the end of cycle 1 the garbage patch and most of its details (such as mesoscale filaments) have been already formed and didn't change during the next six cycles during which the magnitude of concentrations increased by 60%.

Note that, consistent with our assumptions, coastal sources are hard to see on the maps of the saturated solution suggesting that their details are not important.

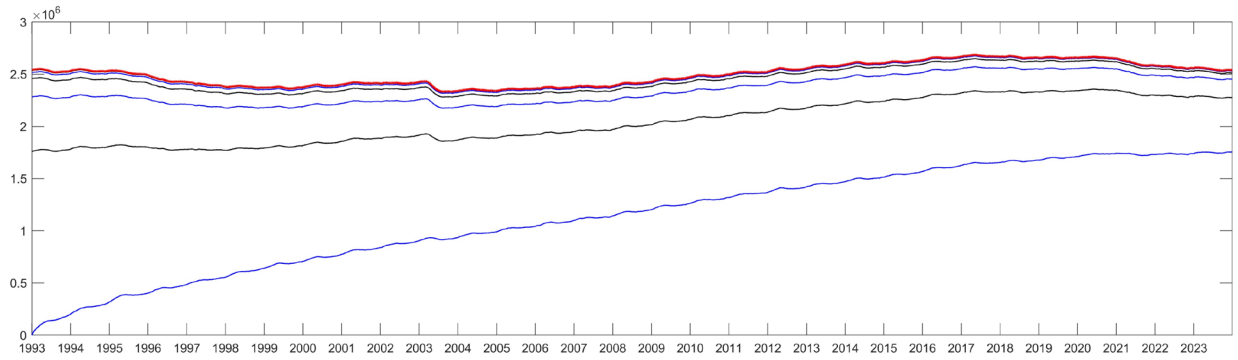


Figure 7. Changes in the total amount of model tracer with time during seven cycles of simulations. The red line shows the saturated solution. Units are model units.

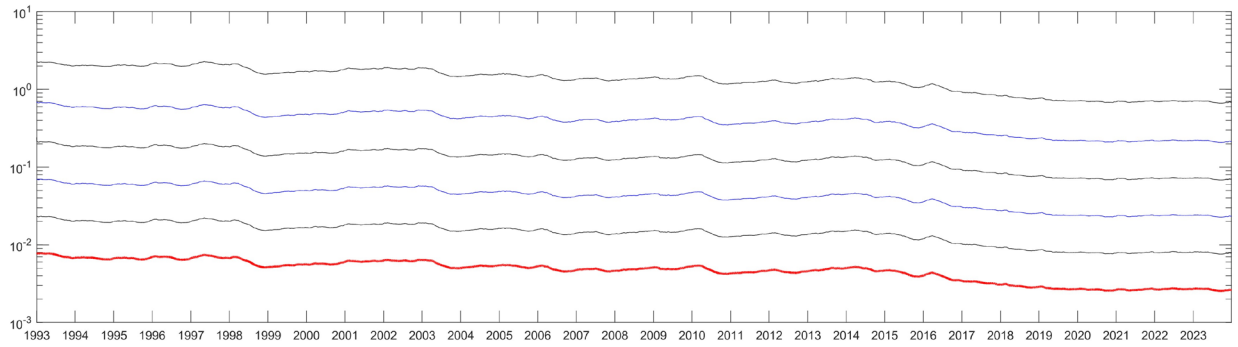


Figure 8. Changes in the root-mean-squared differences in tracer concentrations during pairs of consecutive cycles of simulations. The red line shows the r.m.s. concentration difference between model solutions in cycles 7 and 6. The vertical axis scale is logarithmic.

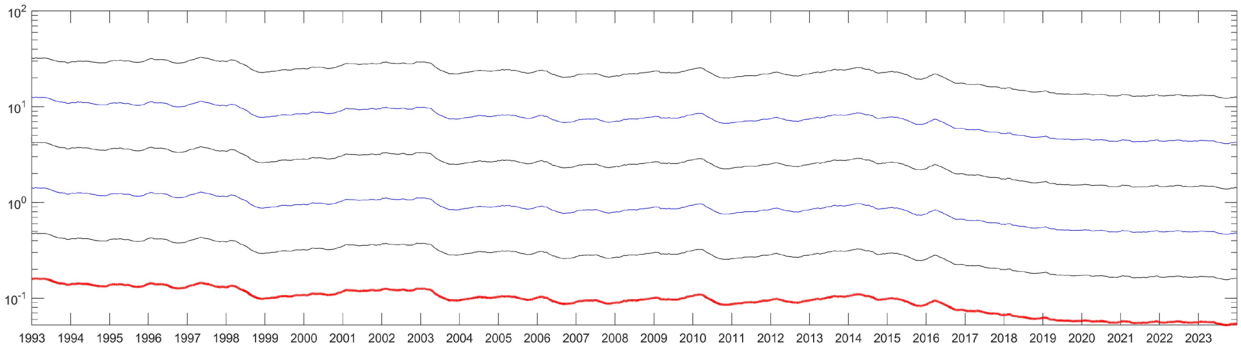


Figure 9. Same as Figure 8 but with r.m.s. differences scaled to the average tracer concentration calculated for the same time moment.

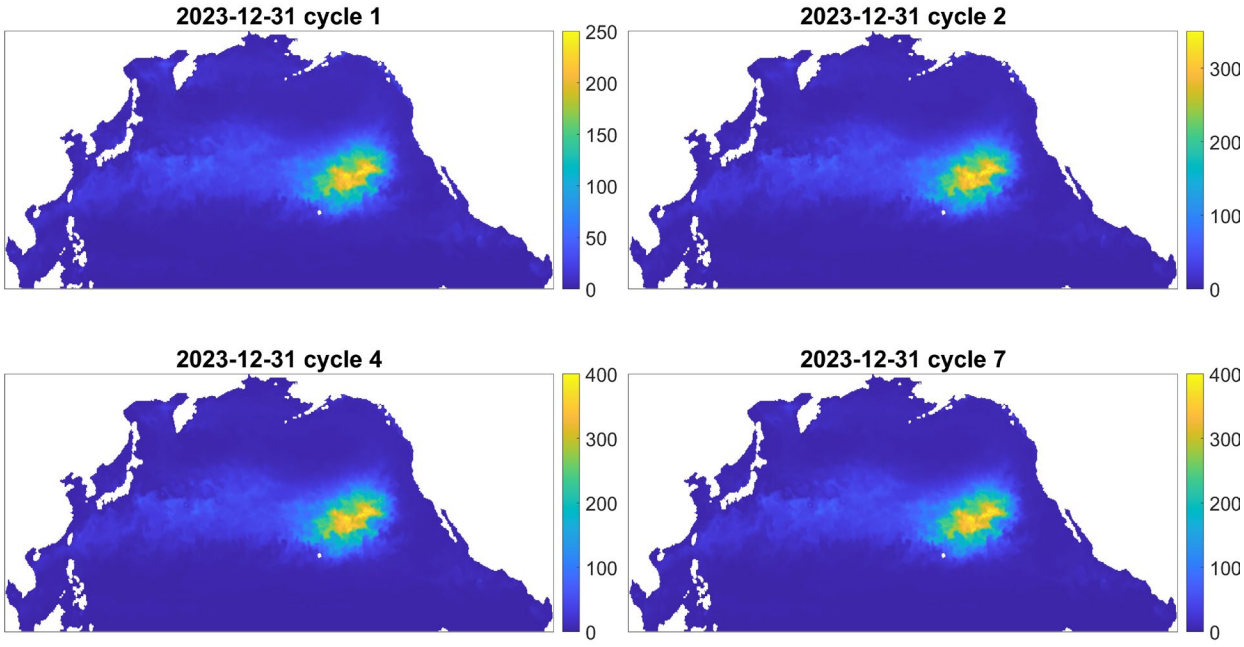


Figure 10. Saturation of the "garbage patch" pattern and magnitude. Note that the pattern was captured already after the 1st cycle while magnitude of concentration continued increasing in new cycles (changes in color scales).

4. Near-real time product

Results of the saturation experiment are used in forward integrations to provide a near-real time product to inform stakeholders working on Hawaiian Islands and in the eastern North Pacific Ocean.

4.1 Access to the Google Drive and folder structure

The product, zoomed in the eastern North Pacific, is available through the Google Drive at

https://drive.google.com/drive/folders/1-8SOxKkpLoyqQYb5UaoVknZLrMn9HPzn

The product is public, and all materials collected in this folder can be downloaded but no changes are permitted, and Google may require authentication at the entrance.

Files in the GFolder include:
yyyy-mm-dd-concentration.jpeg, yyyy-mm-dd-anomaly.jpeg, and Timeline365days.jpeg
where yyyy is year, mm is month, and dd is day. The product also includes a subfolder "Archive" storing previous maps.

yyyy-mm-dd-concentration.jpeg is a map of tracer concentration, calculated with the model described above. An example of such a map is shown in Figure 11, which indicates the garbage patch position north-northeast of Hawaii and highlights several filaments extending toward the islands.

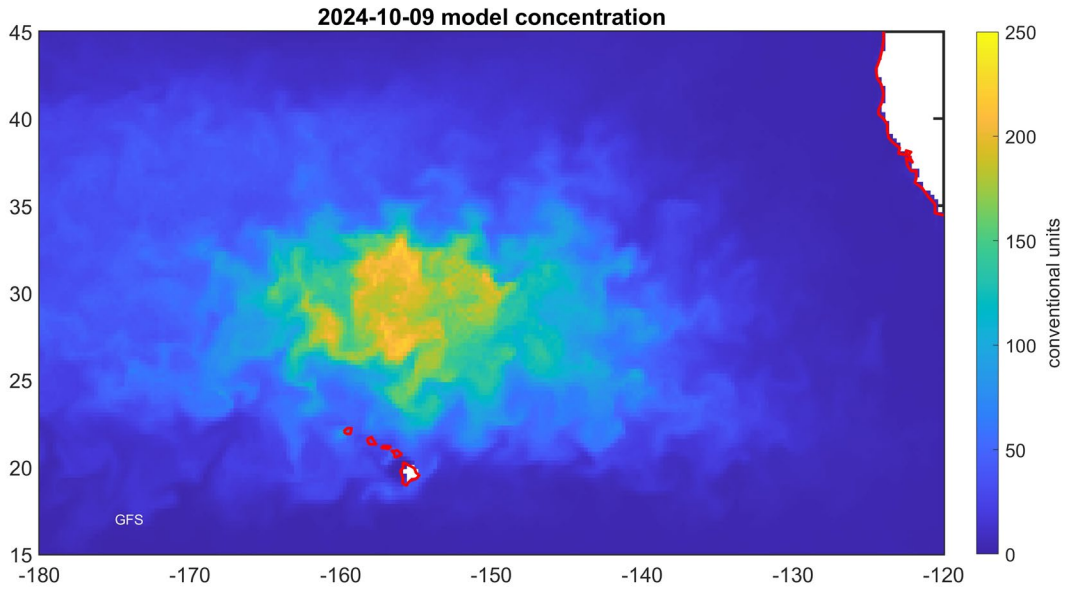


Figure 11. Example of model concentration map for October 9, 2024, provided as a part of the product.

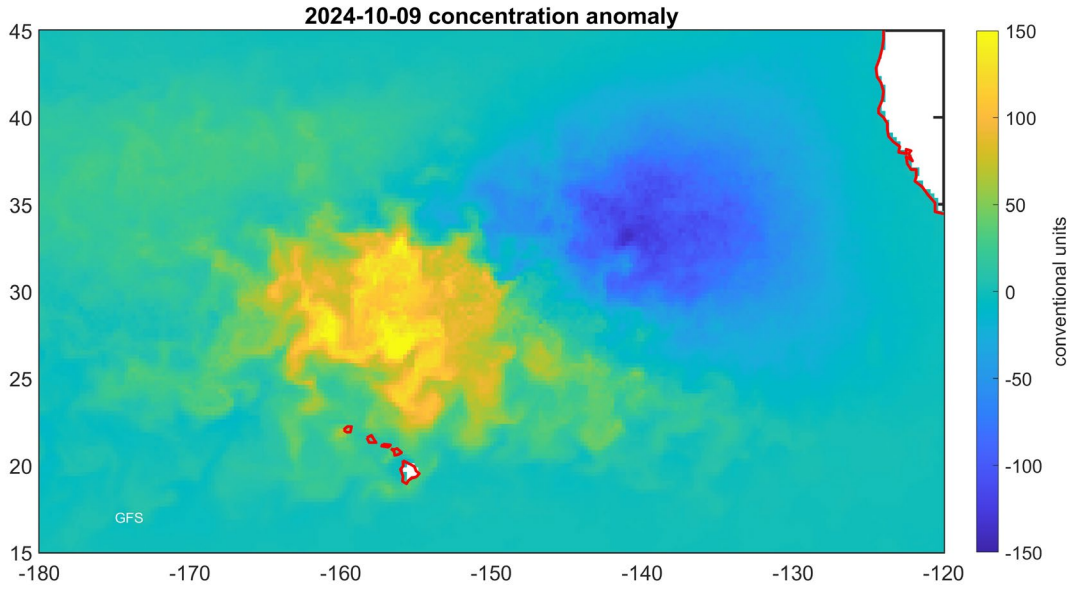


Figure 12. Example of model concentration anomaly map for October 9, 2024, provided as a part of the product.

yyyy-mm-dd-anomaly.jpeg is a map obtained by subtracting from the present tracer concentration the mean concentration averaged over a 31-year period (1993-2023). An example of such a map is shown in Figure 12. Strong positive anomaly near Hawaii and equally strong negative anomaly near the US West Coast indicate that the current location of the garbage patch is shifted west-southwest from its average position. This suggests an anomalously high influx of debris on Hawaiian coastlines, confirmed by local cleanup organizations.

Additionally, model indices, derived for the Northwestern Hawaiian Islands, Kauai, Oahu, Maui, and Hawaii as described in Section 5.3 are updated in Timeline365days.jpeg (Figure 13). Different colors are used for different islands or groups of islands, the timelines include model data for previous 365 days and 30-day future projections.

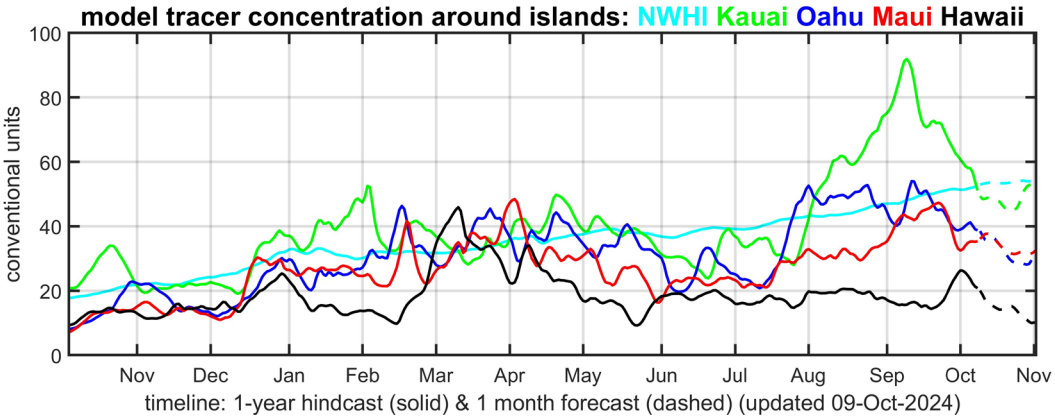


Figure 13. Example of timelines of tracer concentrations near main (Kauai, Oahu, Maui, and Hawaii) and (Northwestern; NWHI) Hawaiian Islands updated October 9, 2024, and included in the product. Solid lines of respective colors show changes of concentrations over the past 365 days. Dashed lines reflect a 30-day forecast as described in Section 5.3.

4.2 Algorithm for updates

Daily updates are initiated at 10am HST and usually finish before 11am.

i. New AVISO, ERA5/ECMWF, and GFS data are downloaded, quality-checked, and reformatted.
ii. Model solution is updated. ERA5 data are treated as higher quality than GFS, so simulations start from the most recent (usually 7-day old) solution totally based on ERA5 and continue to the end of the ERA5 dataset (usually 6 days before present). Next, integration continues to the present using GFS winds. Use of GFS is indicated in the left corner of corresponding maps (e.g., see Figures 11 and 12). The model maps for the days involved in the update are also updated in the Archive subfolder.
iii. A simplified forecasting methodology is developed to project into the near future the model solution under forcing conditions (wind and sea level) resembling the preceding period. For

this, the data of tracer velocities in the last 30 days are reversed in time (not in velocity direction), so that "forecast" velocities N days from the present coincide with the velocities N days before the present. The important property of this method is the consistency between velocity characteristics before the recent past and the near future.

iv. Updated model solutions are used to plot the new timelines.

4.3 Island indices

The ¼-degree model grid is too coarse to adequately represent the bathymetry of most Hawaiian Islands. In practice, only a part of Big Island (Island of Hawaii) is masked in the model as land, all other islands are treated as ocean and tracer velocities are interpolated over their locations. Island indices are calculated as model tracer concentrations averaged over the areas shown in Figure 14. Berg et al (2024) demonstrated good correspondence of such indices with coastal cleanup data collected in 2013-2022. This correspondence results from the dominant role of the northeasterly trade winds bringing most debris to the windward sides of the islands. The influx in this case is proportional to the offshore debris concentration upstream of the wind.

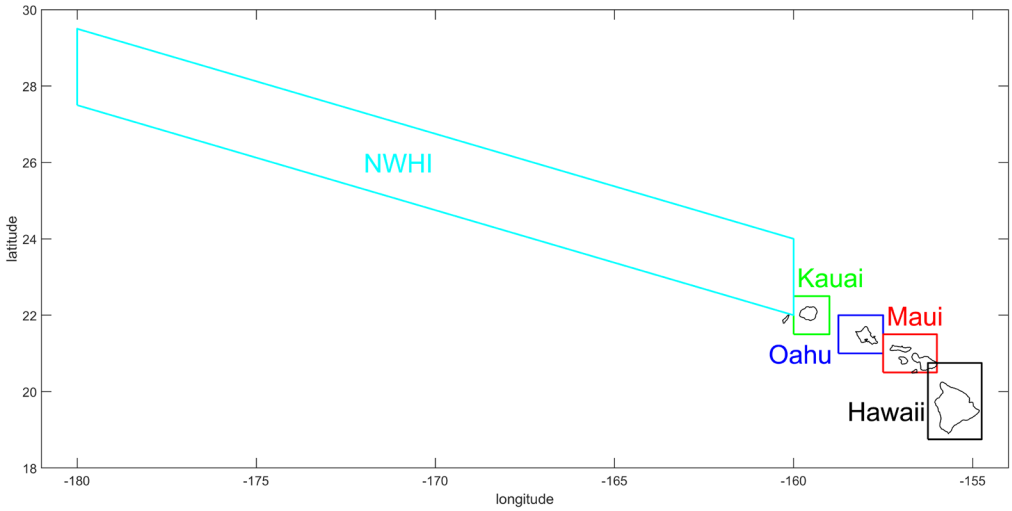


Figure 14. Location of boxes used to derive island indices. Colors are the same as in Figure 13 and in the product.

5. Utility and limitations of the product

Comparisons with coastal (Berg et al, 2024) and at sea (FloatEco project, paper in preparation) data prove the validity of the large-scale pattern and interannual variations of influx to Hawaii of a specific type of debris – derelict fishing gear (DFG). By mass, DFG constitutes the majority of plastic debris observed in the garbage patch or found on Hawaiian shorelines. It is also one of the types having the strongest impact on marine life (entanglement and transport of alien species) and coral reef. The product documents the large "wobbling" of the garbage patch, with its center

shifting east-west by thousands of miles, which provides useful information for a long-term planning of cleanup operations and scientific research.

In many cases, smaller scale, higher frequency phenomena produced by the model were found consistent with observational reports. However, with the complex mesoscale ocean dynamics, under-resolved ocean eddies, and simplistic island concept, such signal should be used with caution. The model does not address such even smaller scale transient phenomena as windrows and fronts, in which the highest concentrations of debris were occasionally reported.

The model focuses on old debris and does not include into consideration relatively "fresh" debris even if locations and times of releases are known. The model is fed by sources constant in time, so the product excludes temporal trends expected due to the fast-growing plastic production. Finally, due to the intense mixing in the garbage patch patterns and beaching events of different types of debris often coincide. However, some types of debris (such as microplastics) may move somewhat differently and form different patterns.

6. Feedback and requests

We are interested in your feedback that would help to validate and improve our product as well as expand its utility to new applications. Please email your comments and requests to

Dr. Nikolai Maximenko <maximenk@hawaii.edu>

7. Acknowledgements

This work was partly supported by the U.S. National Oceanic and Atmospheric Administration Sea Grant through its support of "Nets to Roads: Innovative Research to Scale-Up Removal and Repurposing of Derelict Fishing Gear" and by the U.S. National Aeronautics and Space Administration (grant 80NSSC17K0559) through membership in Biological Diversity & Ecological Forecasting and Ocean Surface Topography Science Teams. We acknowledge help from the FloatEco team, especially Ms. Mary Crowley (Ocean Voyages Institute) and partners from HI-MDAP who helped to justify and validate our product. We also thank Dr. Jennifer Lynch and her team at the Hawaii Pacific University's Center for Marine Debris Research leading the "Nets to Roads" project, collaboration with whom motivated our effort.

8. Citation

Please cite this paper as follows.

Maximenko, N., and J. Hafner, 2024, Near-real time model product to support marine debris research *and operations in Hawaii and in the eastern North Pacific, IPRC Technical Note No. 7, October 20, 2024, 17pp. (available at https://iprc.soest.hawaii.edu/publications/tech_notes.php)*

9. References

Carl J. Berg, Jan Hafner, Megan R. Lamson, Nikolai A. Maximenko, Cynthia W. Welti, Interannual variability in marine debris accumulation on Hawaiian shores: The role of North Pacific Ocean basin-scale dynamics, Marine Pollution Bulletin, Volume 203, 2024, 116484, ISSN 0025-326X, https://doi.org/10.1016/j.marpolbul.2024.116484.

Hersbach, H., Bell, B., Berrisford, P., Biavati, G., Horányi, A., Muñoz Sabater, J., Nicolas, J., Peubey, C., Radu, R., Rozum, I., Schepers, D., Simmons, A., Soci, C., Dee, D., Thépaut, J-N. (2018): ERA5 hourly data on single levels from 1940 to present. Copernicus Climate Change Service (C3S) Climate Data Store (CDS), DOI: 10.24381/cds.adbb2d47. (Accessed March 7, 2023)

Maximenko, N.A., and J. Hafner, 2010: SCUD: Surface Currents from Diagnostic model, IPRC Tech. Note 5, 17pp. https://iprc.soest.hawaii.edu/publications/tech_notes/SCUD_manual_02_17.pdf

Maximenko, N.A., J. Hafner, and P. Niiler, 2012: Pathways of marine debris from trajectories of Lagrangian drifters. *Marine Pollution Bulletin*, **65** (1-3), 51-62, doi:10.1016/j.marpolbul.2011.04.016.

Maximenko, N. A., J. Hafner, M. Kamachi, and A. MacFadyen, 2018: Numerical simulations of debris drift from the 2011 tsunami in Japan, verified with boat reports, *Mar. Pollut. Bull.,* 132, 5-25, https://doi.org/10.1016/j.marpolbul.2018.03.056.

Maximenko, N., P. Corradi, K. L. Law, E. Van Sebille, S. P. Garaba, R. S. Lampitt, F. Galgani, V. Martinez-Vicente, L. Goddijn-Murphy, J. M. Veiga, R. C. Thompson, C. Maes, D. Moller, C. R. Löscher, A. M. Addamo, M. Lamson, L. R. Centurioni, N. Posth, R. Lumpkin, M. Vinci, A. M. Martins, C. D. Pieper, A. Isobe, G. Hanke, M. Edwards, I. P. Chubarenko, E. Rodriguez, S. Aliani, M. Arias, G. P. Asner, A. Brosich, J. T. Carlton, Y. Chao, A.-M. Cook, A. B. Cundy, T. S. Galloway, A. Giorgetti, G. J. Goni, Y. Guichoux, L. Haram, B. D. Hardesty, N. Holdsworth, L. Lebreton, H. A. Leslie, I. Macadam-Somer, T. Mace, M. Manuel, R. Marsh, E. Martinez, D. Mayor, M. Le Moigne, M. E. M. Jack, M. C. Mowlem, R. W. Obbard, K. Pabortsava, B. Robberson, A.-E. Rotaru, G. Ruiz, M. T. Spedicato, M. Thiel, A. Turra, C. Wilcox, 2019: Toward the Integrated Marine Debris Observing System, Toward the Integrated Marine Debris Observing System, Front. Mar. Sci., 6:447, doi: 10.3389/fmars.2019.00447.

Maximenko, N., A.P. Palacz, L. Biermann, J. Carlton, L. Centurioni, M. Crowley, J. Hafner, L. Haram, R.R. Helm, V. Hormann, C. Murray, G. Ruiz, A. Shcherbina, J. Stopa, D. Streett, T. Tanhua, C. Wright, and C. Zabin. 2021. An integrated observing system for monitoring marine debris and biodiversity. Pp. 52–59 in Frontiers in Ocean Observing: Documenting Ecosystems, Understanding Environmental Changes, Forecasting Hazards. E.S. Kappel, S.K. Juniper, S. Seeyave, E. Smith, and M. Visbeck, eds, A Supplement to Oceanography 34(4), https://doi.org/10.5670/oceanog.2021.supplement.02-22.

Potemra, J. T., 2012, Numerical modeling with application to tracking marine debris, Mar. Poll. Bull., 65 (2012) 42–50, doi:10.1016/j.marpolbul.2011.06.026

Trinanes, J.A., M.J. Olascoaga, G.J. Goni, N.A. Maximenko, D.A. Griffin, and J. Hafner, 2016: Analysis of potential MH370 debris trajectories using ocean observations and numerical model results. *Journal of Operational Oceanography*, **9** (2), 126-138, doi:10.1080/1755876X.2016.1248149.